batteries

MDPI

Article

Assessing Solid Products in Nonaqueous Lithium-Oxygen Batteries Using Advanced Neutron Tomography and Titration Techniques †

Helen Ma [1], Amirhossein Sarabandi [1], Yousof Nayfeh [1], Yuxuan Zhang [2] and Xianglin Li [1,*]

[1] Department of Mechanical Engineering and Materials Science, Washington University in St. Louis, St. Louis, MO 63130, USA
[2] Neutron Scattering Division, Oak Ridge National Laboratory, Oak Ridge, TN 37831, USA
* Correspondence: lxianglin@wustl.edu; Tel.: +1-(314)-935-3249

† This manuscript has been authored by UT-Battelle, LLC, under contract DE-AC05-00OR22725 with the US Department of Energy (DOE). The US government retains and the publisher, by accepting the article for publication, acknowledges that the US government retains a nonexclusive, paid-up, irrevocable, worldwide license to publish or reproduce the published form of this manuscript, or allow others to do so, for US government purposes. DOE will provide public access to these results of federally sponsored research in accordance with the DOE Public Access Plan (http://energy.gov/downloads/doe-public-access-plan, accessed on 24 March 2026).

Abstract

This project investigates how the orientation of the carbon cathode with a single-sided microporous layer (MPL) affects battery performance through electrochemical tests, neutron tomography, and titration experiments. The titration experiment quantitatively assesses the amount of solid product (Li_2O_2) deposited on the electrode surface. In addition, neutron imaging with a 16 µm voxel resolution provides details on the spatial distribution of the solid product within the porous electrodes. Additionally, the performance impact of two electrolyte solvents, tetra ethylene glycol dimethyl ether (TEGDME) and dimethyl sulfoxide (DMSO), is evaluated when used to soak the carbon cathode. The cathode orientation where the MPL faces toward the electrolyte and separator reaches higher discharge and charge capacities and greater average discharge voltages compared to when the MPL faces away from the separator. Batteries discharged with DMSO as the solvent have a 64.86% decrease on average in discharge capacity compared to batteries using TEGDME as the solvent. Both the titration experiments and neutron imaging confirmed that the amount of solid products exhibits a linear correlation with the discharged capacity. Additionally, electrolytes with a high donor number, such as DMSO, were found to result in a smaller amount of Li_2O_2 deposited on the electrode surface.

Keywords: Li-O_2 battery; Li-Air battery; neutron tomography; titration; mass transfer; current density; cell orientation

Check for updates

Academic Editors: Pascal Venet and Seung-Wan Song

Received: 27 February 2026
Revised: 25 March 2026
Accepted: 26 March 2026
Published: 29 March 2026

Copyright: © 2026 by the authors. Licensee MDPI, Basel, Switzerland. This article is an open access article distributed under the terms and conditions of the Creative Commons Attribution (CC BY) license.

1. Introduction

With rapidly increasing global energy demand, lithium-oxygen (Li-O_2) batteries have become increasingly popular to help mitigate environmental issues, such as climate change and air pollution. Li-O_2 batteries are a type of metal–air battery with a high theoretical specific energy of 3500 Wh/kg, based on the formation of lithium peroxide (Li_2O_2) as the discharge product [1,2]. One of the most well-known energy storage devices, the lithium-ion (Li-ion) battery, will have an increasingly energy intensive extraction of raw

materials used in production, and has a lower theoretical specific energy of 250 Wh/kg and a practical value of 160 Wh/kg [3,4]. Despite the high theoretical specific energy of Li-O_2 batteries, there are still critical challenges that limit their practical applications. One major issue is the poor cycle life due to cycling inefficiencies and degradation of performance from repeated discharge–charge cycles [5]. The poor rate capability is another issue that may be a result of pore clogging and electrode surface passivation, which reduces material transport capabilities [6]. Additionally, compared to Li-ion batteries, which have a round-trip efficiency of >95%, nonaqueous Li-O_2 batteries have a significantly lower round-trip efficiency of <70% [7,8].

Laoire et al. [9,10] suggest that the electrochemical reactions that occur in a Li-O_2 battery follow the reactions shown in Equations (1)–(3). The reduction of the oxygen that occurs at the cathode yields lithium superoxide (LiO_2):

$$O_2 + Li^+ + e^- \rightarrow LiO_2 \quad (1)$$

This is followed by a disproportionation reaction, Equation (2) and/or Equation (3):

$$2LiO_2 \rightarrow Li_2O_2 + O_2 \quad (2)$$

$$LiO_2 + Li^+ + e^- \rightarrow Li_2O_2 \quad (3)$$

These reactions produce lithium peroxide, the main discharge product. Adams et al. [11] have demonstrated that the discharge current density influences Li_2O_2 formation, thus affecting battery performance and capacity. Lower current densities result in the clustering of Li_2O_2 nanocrystallites on the electrode surface, while higher current densities lead to thin films. Furthermore, as current densities increase, overall discharge capacities were found to decrease. Kwak et al. [1] summarize that high-donor-number (DN) solvents, such as DMSO, avoid passivation of the electrode surface, which results in higher rates and capacities, compared to low-DN solvents such as TEGDME. Lee et al. [12] used a UV–visible titration analysis to determine that less Li_2O_2 is formed on cathodes in DMSO solutions compared to TEGDME solutions at the same capacity, confirming that higher-DN solvents promote Li_2O_2 formation in the electrolyte solution rather than on the electrode surface. Sharon et al. [13] determined that, along with the DN of the solvent, the anion has a strong influence on the oxygen reduction reaction (ORR). However, using a strongly dissociated salt, such as LiTFSI, forms solvated complexes where the Li cation is primarily solvated by the solvent and has minimal interaction with the TFSI anion.

Gittleson et al. [14] reported that the diffusion coefficient of oxygen in TEGDME solutions is multiple orders of magnitude lower than in DMSO solutions. Additionally, TEGDME solutions exhibit greater variance, suggesting a stronger dependence on salt concentration and anion type. Specifically, they found that the oxygen diffusion coefficient of 1 M LiTFSI/DMSO is 1.09×10^{-5} cm^2/s, while for 1 M LiTFSI/TEGDME it is 1.60×10^{-7} cm^2/s. The physical properties of different solvents and electrolytes are also reported in our previous publication [15].

In this paper, the discharge and charge capacities are analyzed for two different cathode orientations, electrolyte solvents (DMSO vs. TEGDME), and different operating current densities (0.1–0.5 mA/cm^2) using commercial carbonaceous electrodes. The dependence of the lithium peroxide content on the cathode orientation, electrolyte solvent, and operating current density is determined using the UV–visible titration analysis. While titration experiments provide quantitative bulk measurements of solid products (Li_2O_2) accumulated on electrode surfaces, they provide no information on the spatial distributions of these products within the porous electrode. Therefore, we quantitatively measured the spatial

distribution of lithium products using advanced neutron tomography with high voxel resolutions (~48 μm). This capability allows us to answer a fundamental question that cannot be addressed by bulk measurements alone: the uniformity of electrochemical reactions across the electrode, and whether reactions favor regions with more sufficient oxygen or ion transport. By correlating spatial variations in Li_2O_2 concentration with electrode architecture (e.g., channel versus rib regions) and electrolyte properties (TEGDME versus DMSO), neutron tomography provides critical insights into how transport limitations govern reaction uniformity, which is essential for validating battery models and guiding electrode design. With these complementary tools, our analyses consider the varying oxygen concentrations and effective diffusivities in the electrolyte, providing quantitative insight into the transport phenomena within porous electrodes. The results from this study offer critical information for both battery design and scientific battery models.

2. Materials and Methods

2.1. Single-Cell Battery Preparation

Anode: A lithium metal chip is used as the anode. The lithium chip is 15.6 mm in diameter and 0.25 mm in thickness. Based on a theoretical specific capacity of 3860 mAh/g, a density of 0.534 g/cm^3, and a thickness of 0.25 mm, the lithium chip can provide a capacity of approximately 51.54 mAh/cm^2. This capacity is significantly higher than that achieved by any of the batteries; therefore, the lithium anode is not the limiting factor governing the discharge capacity.

Electrolyte and separator: Two different solvents are used: tetra ethylene glycol dimethyl ether (TEGDME, Sigma-Aldrich, St. Louis, MO, USA) and dimethyl sulfoxide (DMSO, Sigma-Aldrich, St. Louis, MO, USA). Two different electrolytes are prepared by dissolving 1 mol/L Bis(trifluoromethane)sulfonimide lithium salt (LiTFSI 99.95%, Sigma-Aldrich, St. Louis, MO, USA) in solvent in the glove box. For each electrolyte, a different separator is selected and prepared.

For TEGDME, a Celgard 2500 (25 μm thickness) separator is used. The separator is punched into a 3/4 in (19.05 mm) diameter circle. The separator is soaked in 1 M LiTFSI/TEGDME electrolyte overnight to ensure that the separator is fully wetted. Due to the significantly higher surface tension of DMSO compared to TEGDME (42.9 vs. 30.3 mN/m [16]), the Celgard separator cannot be properly wetted by the DMSO electrolyte, which adversely affects the battery performance and consistency of test results. Consequently, a Whatman glass microfiber (Whatman GF/B, Cytiva, Marlborough, MA, USA, 21 mm diameter, CAT No. 1821-021) is used with the DMSO electrolyte. A total of 100 μL of 1 M LiTFSI/DMSO electrolyte is pipetted onto the separator.

Cathode: Carbon cloth with a microporous layer (CeTech Carbon Cloth with MPL—W1S1011, Fuel Cell Store, Bryan, TX, USA) is used as the cathode throughout this study. The carbon cathode has a thickness of 0.41 mm and a mass of 20 mg/cm^2. It is punched into 1/2 in (12.7 mm) diameter circles. The cathode is soaked in an electrolyte, either 1 M LiTFSI/TEGDME or 1 M LiTFSI/DMSO, overnight to ensure that the cathode is adequately wet.

Assembly: All batteries are assembled in an argon-filled Vacuum Technology glovebox with O_2 and H_2O concentrations maintained below 0.1 ppm. The battery frames are custom-designed and made from 316 stainless steel with parallel flow channels with a size of 0.9 × 0.9 cm^2. Details of the battery frame can be found in our previous publications [2,17]. The areal capacity calculations in this study are based on an area of 1.27 cm^2, corresponding to a 1/2-inch-diameter disk.

2.2. Discharge/Charge Experiments

All batteries are discharged and charged at constant current densities using a Neware CT-4008Tn-5V10mA battery cycler (Neware, Shenzhen, Guangdong, China). The oxygen flow is controlled using a flow meter from Airgas. The oxygen flow rate is set to 5 cubic centimeters per minute (ccm). All experiments are performed at room temperature. A 2 h rest period was applied prior to discharging. The batteries were discharged with a constant current density of 0.1 mA/cm^2, 0.25 mA/cm^2, or 0.5 mA/cm^2 to a cutoff voltage of 2.0 V. After discharge, a 30 min rest period was applied. The batteries were then charged at a constant current density of 0.1 mA/cm^2 to a cutoff voltage of 4.25 V, followed by a constant voltage charge at 4.25 V to a cutoff current density of 0.05 mA/cm^2. Reported capacities with error bars are averaged over at least three independently assembled cells under identical conditions, with error bars indicating one standard deviation.

2.3. Titration/UV–Visible Spectrophotometry Experiments

A lithium peroxide analysis is performed using a color-changing titration that is analyzed using a UV–visible spectrophotometer (Varian Cary 50Bio, Varian, Inc. in Melbourne, Australia) [12]. The water-based titration solution consists of 2% titanium (IV) oxysulfate ($TiOSO_4$, ≥29%, Sigma-Aldrich, St. Louis, MO, USA) dissolved in 1 M sulfuric acid (H_2SO_4, 95.0–98.0%, Macron Fine Chemicals, Avantor, Inc., Radnor, PA, USA).

A control set of experiments was performed using lithium peroxide powder (Li_2O_2, 90%, Sigma-Aldrich) to determine an experimental relationship between the concentration of Li_2O_2 and the absorbance measured by the UV–visible spectrophotometer. Li_2O_2 was measured and mixed into the titration solution. The mixture was then diluted with deionized water (DI H_2O) by a factor of 10 to 30 to obtain a range of Li_2O_2 concentrations. These diluted solutions produce a visible color change as a result of the reactions described below.

$$Li_2O_2 + 2H_2O \rightarrow 2LiOH + H_2O_2 \quad (4)$$

$$TiOSO_4 + H_2O_2 + H_2SO_4 \rightarrow H_2[Ti(O_2)(SO_4)_2] + H_2O \quad (5)$$

Li_2O_2 reacts with H_2O to produce H_2O_2, which then reacts with $TiOSO_4$ and H_2SO_4 to produce $H_2[Ti(O_2)(SO_4)_2]$, a titanium peroxide complex that produces a color on the visible color spectrum [12]. The wavelength and absorbance of the samples were measured using the UV–visible spectrophotometer. Diluting the solution is an important step to ensure that the absorbance measured by the UV–visible spectrophotometer does not exceed 1 absorbance unit (AU). The relationship between Li_2O_2 concentration and absorbance measured by the UV–visible spectrophotometer was determined using ten controlled amounts of Li_2O_2 powder mixed with the titration solution. Multiple trials were conducted to ensure repeatability. The absorbance as a function of the Li_2O_2 concentration is plotted in Figure 1a. The peak absorbance follows a nearly linear relationship with the Li_2O_2 concentration [mol/L], as shown in Figure 1b. This linear relationship between Li_2O_2 concentration and absorbance is used to determine the amount of Li_2O_2 content in discharged cathode samples.

Li_2O_2 content in cathode samples was measuring using the experimentally determined relationship between absorbance and Li_2O_2 mass (Figure 1). The cathodes were first washed using anhydrous acetonitrile (AN, 99.8%, Millipore Sigma) to avoid the decomposition of H_2O_2 by DMSO. The cathodes were then dried, soaked in 3 mL of the titration solution, and sonicated in an ice bath for at least 15 min to ensure that the Li_2O_2 in the cathode fully reacted. The mixture was then diluted with DI H_2O until the mixture was a visibly light-yellow color. The wavelength and absorbance were measured using the UV–visible spectrophotometer.

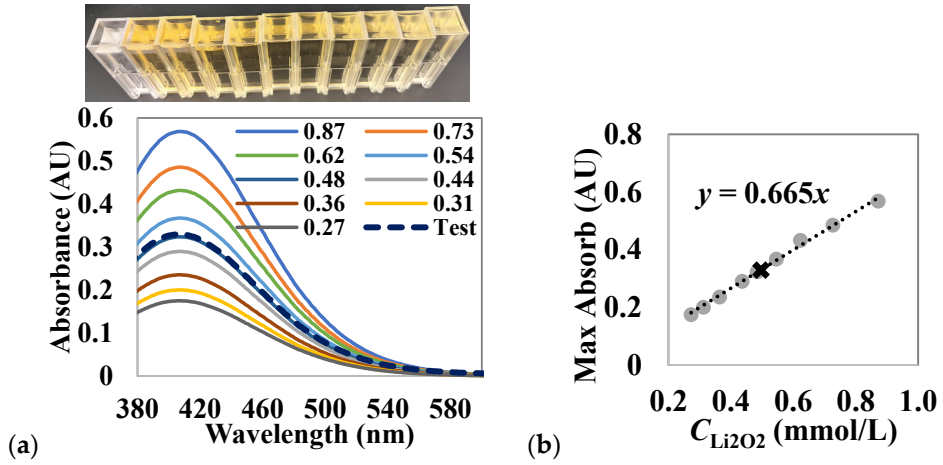


Figure 1. (**a**) Wavelength vs. absorbance for nine controlled concentrations of Li_2O_2 (in mmol/L) and one electrode sample with unknown Li_2O_2 concentration ("Test"). The photo on top shows images of solutions with decreasing Li_2O_2 concentrations from left to right (the leftmost sample is pure H_2O used as the baseline). (**b**) Peak absorbance as a function of controlled concentrations of Li_2O_2 and the location of the tested sample (black cross).

2.4. Neutron Tomography

Neutron computed tomography (CT) was performed at the Multimodal Advanced Radiography Station (MARS) at the High Flux Isotope Reactor (HFIR), Oak Ridge National Laboratory, Oak Ridge, TN, USA [18]. Moderated and collimated neutrons with wavelengths ranging from 0.8 to ∼6 Å with a peak around 2.6 Å were used for this measurement. The beamline provides a collimation L/D ratio of between 400 and 2000, where L is the distance of the collimator from the aperture, and D is the diameter of the aperture. All measurements used an L/D ratio of 600. A 40 µm Gd_2O_2S:Tb scintillator screen was used to convert the transmitted neutrons into light signal, which was recorded by a scientific Complementary Metal-Oxide-Semiconductor (sCMOS) camera (QHY600, QHYCCD, Beijing, China) as a 2D gray-scale radiograph [19]. The effective pixel size in collected radiograph is about 16 µm. For the CT scan, the samples were mounted on a stage which rotated 360°. In this work, one projection was taken in rotation steps of 0.14° with a 30 s exposure time. After conducting the CT scan, post-processing including background normalization, outlier removal (3 × 3 kernel size), ring artifact removal, and volume reconstruction (Simultaneous Iterative Reconstruction Technique) were performed using in-house developed tools based on Algotom [20], TomoPy [21], and *bm3d-streak-removal* [22]. 3D visualization and analysis were completed using Dragonfly 3D World (Version 2025.1) [23].

3. Results

3.1. Impact of Cathode Orientation on Performance

Figure 2 shows a schematic of the two cathode orientations: the microporous layer (MPL) facing away from the separator (MPL Outward) and toward the separator (MPL Inward). These two scenarios used identical electrodes, which are made from MPL coated on carbon cloth, with the only difference being the orientation of the cathode electrode during assembly.

To determine the dependence of the discharge and charge capacity on cathode orientation, batteries with two different cathode orientations were run under the same conditions, as described in Section 2.2. Figure 3a plots voltage as a function of the areal capacity for an MPL Outward and an MPL Inward sample.

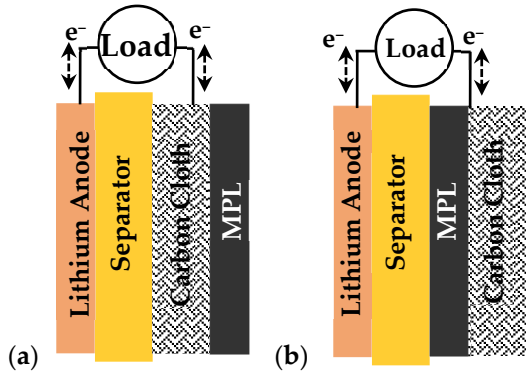


Figure 2. Schematic of a battery with two different cathode orientations. (**a**) The MPL (dark gray) of the carbon cathode faces away from the separator (MPL Outward). (**b**) The MPL of the carbon cathode faces toward the separator (MPL Inward).

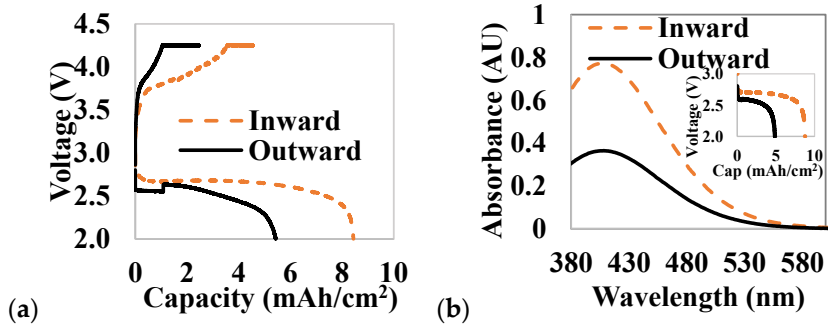


Figure 3. (**a**) Voltage as a function of areal capacity and (**b**) absorbance as a function of wavelength for two cathode orientations: MPL Outward (black) and MPL Inward (orange). Both batteries were discharged and charged at a current density of 0.1 mA/cm^2 using 1 M LiTFSI/TEGDME as the electrolyte.

The areal discharge capacities of the MPL Outward and MPL Inward samples in Figure 3a are 5.44 mAh/cm^2 and 8.44 mAh/cm^2, respectively. After repeating multiple discharge experiments, the average areal discharge capacities were 5.79 ± 3.30 for MPL Outward samples and 7.69 ± 1.13 mAh/cm^2 for MPL Inward samples. These results indicate that the areal discharge capacity of MPL Outward samples is lower than that of MPL Inward samples. Separate discharge experiments were conducted using these two different orientations, and the Li_2O_2 contents of discharged electrodes at the end of discharge were measured using the titration and UV–visible spectrophotometry method. Figure 3b plots absorbance as a function of wavelength for the two cathode orientations, MPL Outward and MPL Inward. The MPL Outward sample has a peak absorbance of 0.37 AU at a wavelength of 408 nm. The MPL Inward sample has a peak absorbance of 0.77 AU at a wavelength of 407 nm. After fitting data generated using controlled concentrations of Li_2O_2 (Figure 1), the amount of Li_2O_2 in the MPL Outward and MPL Inward electrodes were determined to be 1.49 and 3.16 mg, respectively.

It is important to note that the two samples discharged in Figure 3b are different from the two samples discharged and charged in Figure 3a. The discharge capacities of the MPL Outward and MPL Inward samples in Figure 3b are 4.87 and 8.77 mAh/cm^2. The theoretical amounts of Li_2O_2 produced in these samples are 2.65 and 4.77 mg in these two samples, respectively. The mass fractions between the experimental measurement and theoretical Li_2O_2 mass are approximately 56.2% and 66.3%.

While the measured amounts of Li_2O_2 are both lower than theoretical predictions, the titration experiments confirm that the amount of Li_2O_2 correlates with the discharge capacity. Discrepancies between the theoretical estimations and measurements can be at-

tributed to the Li_2O_2 loss caused by sample washing using AN during electrode preparation. Washing the discharged electrodes removes Li_2O_2 formed via the solution deposition mechanism [13,24], and only Li_2O_2 formed on the electrode surface by the surface deposition mechanism could be detected in the titration experiment. The higher mass fraction of the measurable Li_2O_2 in the MPL Inward sample also suggests that the MPL Inward orientation may produce a higher fraction of Li_2O_2 on the electrode surface than in the solution.

It can be seen in Figure 3a that the MPL Outward sample has a lower initial discharge voltage, indicating a higher activation overpotential. The average discharge voltage for the MPL Outward and MPL Inward samples are 2.49 V and 2.61 V, respectively. The areal charge capacities of the MPL Outward and MPL Inward samples in Figure 3a reached 2.44 mAh/cm^2 and 4.54 mAh/cm^2, respectively, suggesting that the MPL Inward orientation allows for higher charge capacities. The columbic efficiencies, defined as the ratio between the charge capacity and the discharge capacity, of the MPL Outward and MPL Inward samples are 44.85% and 53.80%, respectively. The charging activation overpotential on the MPL Outward sample is visually greater, which is supported by the average charging voltage for the MPL Outward sample being greater than that of the MPL Inward sample, at 4.14 V and 4.02 V, respectively.

3.2. Effect of Cathode Orientation on Mass and Ion Transport

The carbon cloth as the substrate has a low surface area and has negligible contributions to the capacities; most reactions occur within the MPL [25]. To confirm this, we conducted experiments using carbon cloths without the MPL as the electrode (Fuel Cell Store, item number W0S1009), which have a thickness of 0.33 mm and a mass of 12 mg/cm^2. Batteries utilizing only carbon cloths without MPL as the electrode showed capacities of less than 0.1 mAh/cm^2 with both electrolytes. When the MPL faces the separator (Inward), the travel distance of the Li^+ from Li metal to the cathode electrode is about 75 μm, which is the sum of the thickness of the separator (25 μm) and half of the thickness of the MPL (100 μm). The oxygen transfer distance through the liquid electrode is about 50 μm, which is half of the thickness of the MPL. In passive cells, both O_2 and Li^+ transfer through battery components by diffusion. The diffusivities of O_2 and Li^+ in TEGDME are 0.217×10^{-9} m^2/s and 0.08×10^{-9} m^2/s [15,26], respectively. The concentration of dissolved O_2 at the air–electrode interface is 1.23×10^{-4} kg/kg (4.43×10^{-3} mol/L); the concentration of the Li^+ in the electrolyte is about 0.26 kg/kg (1 mol/L). The mass flux, N [kg/(m^2·s)], can be calculated from the density of electrolyte, ρ, effective diffusivity, D^{eff} [m^2/s], concentration difference, ΔC, and mass transfer distance, x:

$$N_i = -\rho D_i^{\text{eff}} \frac{\Delta C_i}{x} \tag{6}$$

The maximum mass fluxes for O_2 and Li^+ are 5.33×10^{-7} and 2.77×10^{-4} kg/(m^2·s), respectively. The maximum current density this mass flux can support can be calculated from the mass flux, N, molecular weight, M, number of electrons per molecule, n, and Faradic constant, 96,485 C/mol:

$$i_{\max} = \frac{N_i}{M_i} n_i F \tag{7}$$

The corresponding current densities calculated from the mass balance are 0.32 and 382.3 mA/cm^2, respectively.

In comparison, when the MPL faces the channel (Outward), the travel distance of the Li^+ from Li metal to the cathode electrode is about 300 μm, which is the sum of the thickness of the separator (25 μm), half of the thickness of the MPL (100 μm), and the thickness of the carbon cloth (175 μm). The oxygen transfer distance through the liquid

electrode is still about 50 μm, which is half of the thickness of the MPL. The maximum mass fluxes for O_2 and Li^+ are calculated to be 5.33×10^{-7} and 6.93×10^{-5} kg/(m^2·s), respectively. The maximum current densities calculated from the mass balance are 0.32 and 95.6 mA/cm^2, respectively. The maximum current density of the MPL Inward electrode is about four times as high as the maximum current density of the MPL Outward electrode.

It should be noted that the simplified diffusion-based model makes assumptions for the uniform initial concentration, reaction rate in the electrode, and electrolyte distributions. Despite these assumptions, simplified analysis is valuable for explaining the observed differences between MPL Inward and MPL Outward orientations. To validate the prior analysis of the maximum current density, we performed chronoamperometry tests using two different MPL orientations. The experiment was conducted at a high overpotential, maintaining a constant voltage of 2.0 V, to make sure that the discharge current densities reached the limiting current density constrained by the mass transfer of reactive species. As shown in Figure 4a, the cell with the MPL Inward clearly has a much higher initial discharge current density (35.1 mA/cm^2) than the cell with the MPL Outward (9.65 mA/cm^2). Given the fact that both cells have been saturated by oxygen, the discharge current is proportional to the available Li^+ or ionic conductivity. Since the majority of reaction sites are in the MPL, when MPL faces inward (the separator), the distance for the Li^+ transfer is much shorter than when the MPL faces the channel. As a result, the limiting current density of the MPL Inward electrode is about 3.6 times as high as the limiting current density of the MPL Outward electrode at the beginning of the chronoamperometry test. The roughly fourfold difference in the maximum limited current density measured through chronoamperometry shows a similar trend with the theoretical analysis. While the absolute values of the model predictions may be approximations, the relative comparisons between configurations are robust.

To quantitatively analyze the transport phenomena within the electrode, we conducted EIS measurements of batteries using the Whatman separator before discharge and charge cycles at OCV. Figure 4b shows the Nyquist plots of the two cells with different electrode orientations. The equivalent circuit model (ECM) used to fit the data is shown in Figure 4c. In the ECM, R_0, R_1, C_1, and Z_W represent ohmic resistance, charge transfer resistance, the constant phase element, and the Warburg constant, respectively. The values of parameters fitted based on the EIS data are compared in Table 1. The ohmic resistances, calculated using the high-frequency intercept at the real axis, reflect the ionic resistance of the electrolyte. The significant difference in R_0 between the two orientations (28.7 Ω for MPL Outward versus 18.5 Ω for MPL Inward) confirms that the long travel distance of Li^+ leads to a higher ohmic resistance. Since both experiments used an identical electrolyte, the ionic conductivity, σ, of these two orientations stays the same. The difference in ohmic resistance is proportional to the travel distance of the Li^+. Meanwhile, the charge transfer resistance R_1, associated with the diameter of the semicircle in the Nyquist plot, of the MPL Outward electrode (121.4 Ω) is significantly lower than that of the MPL Inward electrode (356.5 Ω). The lower charge transfer resistance of the Outward orientation indicates more facile electrochemical kinetics, likely due to the balanced access of both Li^+ and O_2 to the reactive sites within the MPL. The Warburg element Z_W, observed as the linear tail at low frequencies, characterizes mass transfer limitations within the electrode. The substantially lower Warburg coefficient for the MPL Outward electrode confirms that the shorter O_2 diffusion path enhances mass transport kinetics. Collectively, these fitted parameters provide quantitative evidence that electrode orientation fundamentally governs both charge transfer kinetics and mass transport characteristics, directly supporting the observed performance differences in the discharge capacity and rate capability.

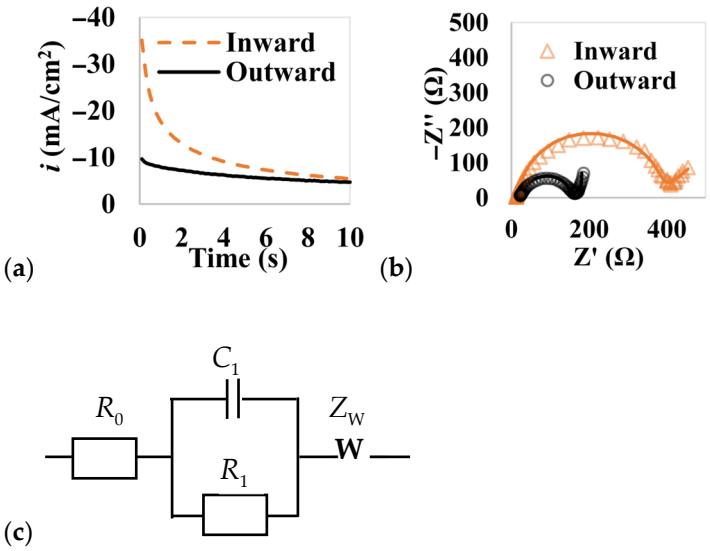


Figure 4. (**a**) Chronoamperometry, (**b**) Nyquist plots at OCV (markers represent the data, while lines are the fitted curves) of electrode tested with 1 M TEGDME and different electrode orientations, and (**c**) the equivalent circuit model to fit the EIS data.

Table 1. Values of fitted parameters in the ECM.

Fitted by Python 3.10.8	R_0 (Ω)	R_1 (Ω)	C_1 (F)	W_0 (Ω)	W_1 (s)
Inward	18.51	356.50	2.47×10^{-5}	513.50	33.07
Outward	28.69	121.40	8.34×10^{-6}	93.80	2.22

3.3. Influence of Electrolyte on Capacity

To determine the dependence of the discharge and charge capacities on the electrolyte solvent, batteries using TEGDME and DMSO as solvents are compared. Figure 5a plots a TEGDME sample and a DMSO sample, both discharged and charged at a current density of 0.1 mA/cm^2. The areal discharge capacities of the TEGDME and DMSO samples in Figure 5a are 8.47 mAh/cm^2 and 2.59 mAh/cm^2, respectively. The areal capacity decreases by 70.96% when the electrolyte is switched from TEGDME to DMSO. The TEGDME sample has a visually higher discharge activation overpotential than the DMSO sample. The average discharge voltage of the TEGDME sample is lower than the DMSO sample at 2.61 V and 2.69 V, respectively, supporting the difference in activation overpotential. Trahan et al. observed a similar pattern of higher discharge voltages in batteries with DMSO-based electrolytes compared to other non-aqueous electrolytes [27].

The areal charge capacities of the TEGDME and DMSO samples are 5.13 and 2.46 mAh/cm^2, respectively, corresponding to a 39.18% decrease. This is evident from the smaller difference between the discharge and charge capacity, suggesting less capacity degradation compared to the TEGDME sample. The coulombic efficiencies of the TEGDME and DMSO samples are 60.57% and 94.98%, respectively. In addition, the charge activation overpotential is visually higher in the TEGDME sample compared to the DMSO sample, with average charge voltages of 4.02 V and 3.56 V, respectively. The lower discharge and charge overpotentials observed with the DMSO-based electrolyte can be attributed to its higher DN compared to TEGDME. The DN of the solvent plays a critical role in stabilizing intermediate species during reactions. High-DN solvents like DMSO strongly solve Li^+ cations, weakening the Li^+-O_2^- interaction and promoting a solution-phase mechanism for Li_2O_2 formation. This solution-mediated pathway leads to faster decomposition during charging, reducing charge overpotential. In contrast, low-DN solvents like TEGDME favor

a surface-mediated mechanism that forms thin, film-like Li_2O_2 layers on the electrode surface, which are more difficult to oxidize and lead to higher charge overpotentials.

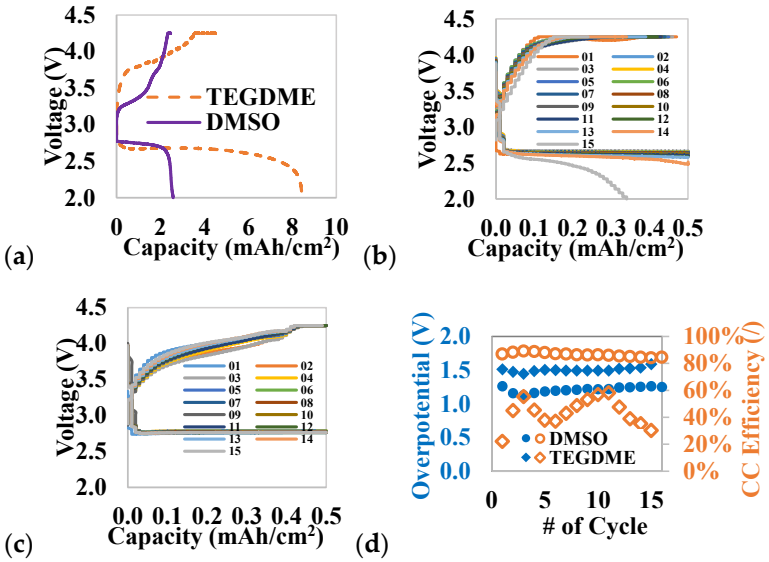


Figure 5. Voltage as a function of areal capacity comparing batteries using TEGDME (orange) and DMSO (purple) as the solvent: (**a**) deep discharged and charged at a current density of 0.1 mA/cm^2 until the cutoff voltages of 2.0 and 4.25V; cycling performance with a cutoff capacity of 0.5 mAh/cm^2 using (**b**) TEGDME and (**c**) DMSO; (**d**) comparisons of the overpotential and columbic efficiency during cycling.

To further elucidate the electrolyte's properties on battery cycling, we performed cycling tests at a fixed capacity of 0.5 mAh/cm^2 with a current density of 0.1 mA/cm^2 and cutoff voltages of 2.0V and 4.25V. Once the charging voltage reaches 4.25V, charging switches to constant voltage charging until the charging current density is less than 0.05 mA/cm^2. This charging protocol follows the constant voltage constant current (CCCV) charging used in many rechargeable batteries. The results in Figure 5b,c show that the DMSO electrolyte can complete more than 15 cycles, all with a 100% coulombic efficiency (defined as the charging capacity divided by the discharge capacity). In contrast, the TEGDME electrolyte only achieves a 94.4% coulombic efficiency on the first cycle, and this efficiency keeps decreasing to 70% by the 15th cycle. The discharge–charge cycle of the TEGDME electrolyte stops at cycle 15 as the discharge voltage reaches 2.0 V, whereas the DMSO electrolyte continues charging beyond the 15th cycle. For clear comparison, we only show the first 15 cycles for both electrolytes in Figure 5d. Additionally, we compared the coulombic efficiency of constant current (CC) charging, which is defined as the charging capacity during CC divided by the discharge capacity. The average coulombic efficiency of CC charging for DMSO is 86.5%, significantly higher than the average of 43.7% for TEGDME. Furthermore, Figure 5d compares the overpotential between discharge and charge. The average overpotential is 1.51 V for TEGDME and only 1.21 V for DMSO. The lower overpotential of the DMSO electrolyte indicates a lower reaction barrier, which is facilitated by the solvent-driven reactions attributed to the high DN of the DMFC.

Furthermore, we discharged batteries with TEGDME and DMSO electrolytes to a capacity of 2 mAh/cm^2, both at a current density of 0.1 mA/cm^2, to investigate the impact of the electrolyte properties on the morphology of discharged Li_2O_2. The top view of discharge electrodes was then analyzed using SEM to visualize the morphological differences between the two electrolytes. As shown in Figure 6, TEGDME tends to form a Li_2O_2 film or small needle-like structures on the surface of the electrode, whereas DMSO results in large and dispersed Li_2O_2 toroid particles in the electrolyte. This observation supports the

understanding that the higher DN of DMSO facilitates solvent-based deposition and Li_2O_2 growth. Additionally, the stronger solvation of Li^+ in DMSO enhances the kinetics of ORR by stabilizing the intermediate, lowering the activation energy for the initial electron transfer and reducing discharge overpotential. These effects collectively explain the improved voltage efficiency observed with DMSO-based electrolytes.

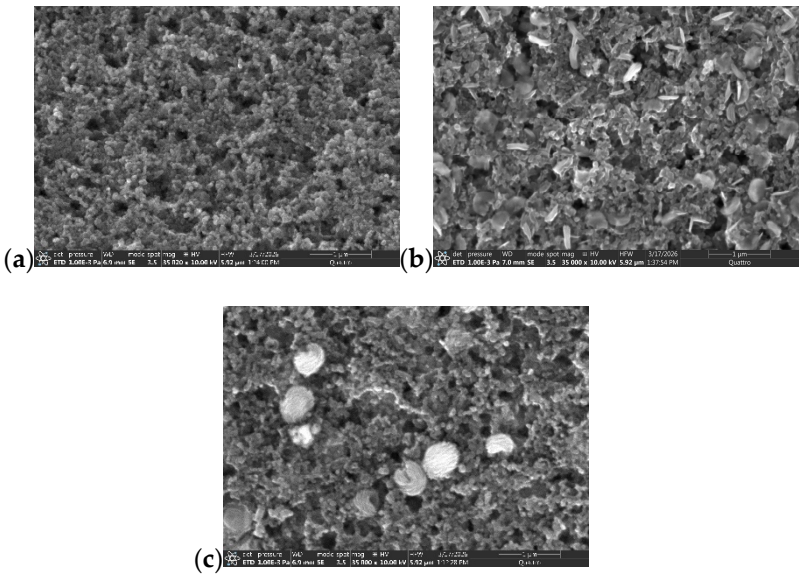


Figure 6. SEM images of (**a**) a fresh electrode and electrodes discharged to 2 mAh cm^{-2} at 0.1 mA cm^{-2} in (**b**) 1 M LiTFSI in TEGDME and (**c**) 1 M LiTFSI in DMSO. All images have a scale bar of 1 μm.

The Li_2O_2 content in the cathodes of a TEGDME and DMSO sample after deep discharge at 0.1 mA/cm^2 was analyzed using the titration and UV–visible spectrophotometry methods. The areal discharge capacities of the DMSO and TEGDME samples in Figure 7 are 4.44 mAh/cm^2 and 8.82 mAh/cm^2, respectively. The theoretical amounts of Li_2O_2 produced in these samples are 2.41 and 4.79 mg, respectively. The DMSO sample has a peak absorbance of 0.176 AU at a wavelength of 404 nm, while the TEGDME sample has a peak absorbance of 0.78 AU at a wavelength of 400 nm. Based on fitting the peak absorbance data from Figure 1, the amount of Li_2O_2 in these two electrodes were estimated to be 0.778 and 3.46 mg, respectively. The mass fractions of the experimentally measured Li_2O_2 to the theoretical Li_2O_2 mass are approximately 32.3% and 72.1%, respectively. The lower mass fraction of the measured Li_2O_2 compared to the theoretical amount in the DMSO sample aligns with the observation that electrolytes with a high DN (such as DMSO) produce a higher fraction of Li_2O_2 in the solution rather than on the surface of the electrode.

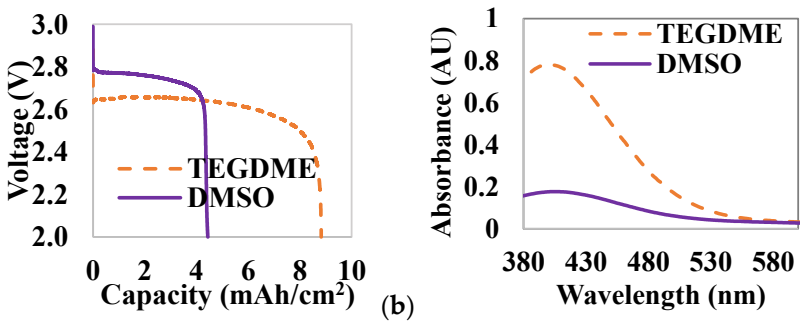


Figure 7. (**a**) Voltage as a function of areal capacity and (**b**) absorbance as a function of wavelength for batteries using 1 M LiTFSI in TEGDME and DMSO electrodes. Both batteries had MPL Inward and were discharged at a current density of 0.1 mA/cm^2.

3.4. Influence of Current Density on Capacity

The discharge curves of TEGDME (Figure 8a) and DMSO samples (Figure 8b) are compared at three current densities: 0.1 mA/cm^2, 0.25 mA/cm^2, and 0.5 mA/cm^2. In Figure 8a, the discharge capacities as current density increases are 9.24 mAh/cm^2, 7.79 mAh/cm^2, and 4.62 mAh/cm^2, respectively. The average discharge voltages as current density increases are 2.61 V, 2.52 V, and 2.42 V, respectively. In Figure 8b, the discharge capacities as the current density increases are 3.65 mAh/cm^2, 2.76 mAh/cm^2, and 1.69 mAh/cm^2, respectively. The average discharge voltages as current density increases are 2.71 V, 2.66 V, and 2.53 V, respectively. Figure 8 has a clear trend that, as current density increases, in both the TEGDME and DMSO samples, the discharge capacity decreases and the activation overpotential increases. A similar trend is seen by Adams et al., which determined that the increasing discharge current density decreases the discharge capacities due to the difference in Li_2O_2 morphology [11].

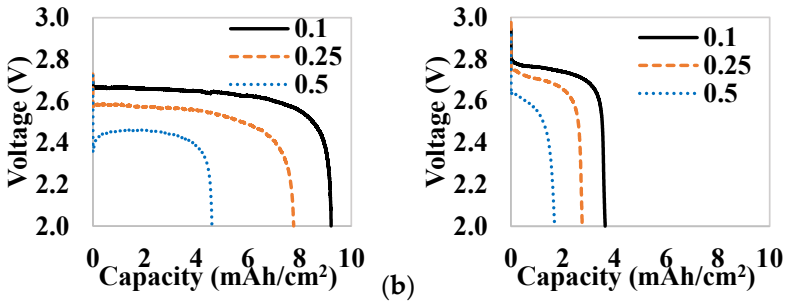


Figure 8. Voltage as a function of areal capacity, comparing increase in discharge current density (mA/cm^2) for (**a**) TEGDME electrolyte solvent and (**b**) DMSO electrolyte solvent.

While batteries using the DMSO electrolyte have a lower activation overpotential compared to batteries using the TEGDME electrolyte, the DMSO electrolyte results in a significantly lower discharge capacity compared to TEGDME at all current densities, as can be seen in Figures 5 and 8. Batteries using the DMSO electrolyte were reported to have higher discharge capacities compared to the TEGDME electrolyte [14,27–30]. However, as seen in Figures 5 and 8, our test data suggest batteries using the TEGDME electrolyte have much higher discharge and charge capacities than batteries using the DMSO electrolyte. The discrepancy could be the result of a difference in the amount of electrolyte within the carbon cloth cathodes. The surface tensions of TEGDME and DMSO at 25 °C are 33.74 mN/m and 42.86 mN/m, respectively [31]. Due to the higher surface tension of DMSO, the DMSO electrolyte struggles to wet porous cathode electrodes. Our contact angle measurements indicate that the DMSO electrolyte generally forms a non-wetting sphere on the electrode surface, while the TEGDME electrolyte is rapidly absorbed by the same porous electrode in less than a second. Even after soaking the electrode overnight in DMSO electrolyte, it is likely not fully wet. Consequently, the liquid saturation in a cathode with DMSO is lower than in one with TEGDME.

To quantitatively assess the differences in wetting behavior between the two electrolytes, we measured the contact angles of pure TEGDME and DMSO on a PTFE sheet using a goniometer (ramé-hart Model 250) under atmosphere condition. TEGDME had a contact angle of 101.75° ± 2.55°, while DMSO exhibited a contact angle of 118.45° ± 3.75°. These measurements align with our observations that TEGDME more easily wets porous battery electrodes and separators compared to DMSO. Consequently, the capacity difference between TEGDME and DMSO can be partially attributed to differences in wetting and saturation. Our previous study quantitatively assessed how electrolyte saturation affects battery performance. The test results from this study suggest that, for typical porous

cathodes with PTFE binders, maintaining a relatively high electrolyte saturation (>40%) remains a challenge, hindering the discharge and charge performance of the battery. A hydrophilic cathode, on the other hand, would result in more similar saturation levels of the cathodes and potentially produce significantly different results.

3.5. Neutron Imaging of Selected Electrodes After Discharging

Neutron tomography of discharged battery electrodes can reveal the spatial distribution of lithium products (mainly Li_2O_2). We measured the neutron tomography of discharged electrodes using ORNL's MARS instrument. The high-resolution tomography (~48 μm) provides a 3D distribution of neutron attenuation coefficient, which is directly related to element concentration within the material. The neutron attenuation coefficient of lithium (^{nat}Li) is significantly higher than that of C, H, and O. As a result, the spatial distribution of the neutron attenuation coefficient within the sample is proportional to the concentration of lithium salts. The spatial distribution of lithium salts within porous cathode electrodes after battery discharge allows us to observe the distribution patterns throughout the electrode material.

A higher attenuation coefficient indicates a higher concentration of lithium salts. Regions of high lithium product accumulation indicate higher cumulative discharge reactions, while regions of lower lithium product accumulation indicate lower cumulative discharge reactions. The top views of the discharged electrodes at 0.1 mA/cm^2 (Figure 9a) clearly show patterns of the gas channels. The absorption intensities, which are directly proportional to lithium salt concentration, in the channel areas are higher than those outside the channels, indicating higher concentrations of Li_2O_2. This suggests higher cumulative reaction rates under the channels due to more effective O_2 transfer. Such spatial heterogeneity cannot be detected through electrochemical measurements or titration alone, which average across the entire electrode. Neutron tomography thus uniquely reveals how electrode architecture and operating conditions create localized reaction hot spots. This insight is critical for designing electrodes with more uniform utilization.

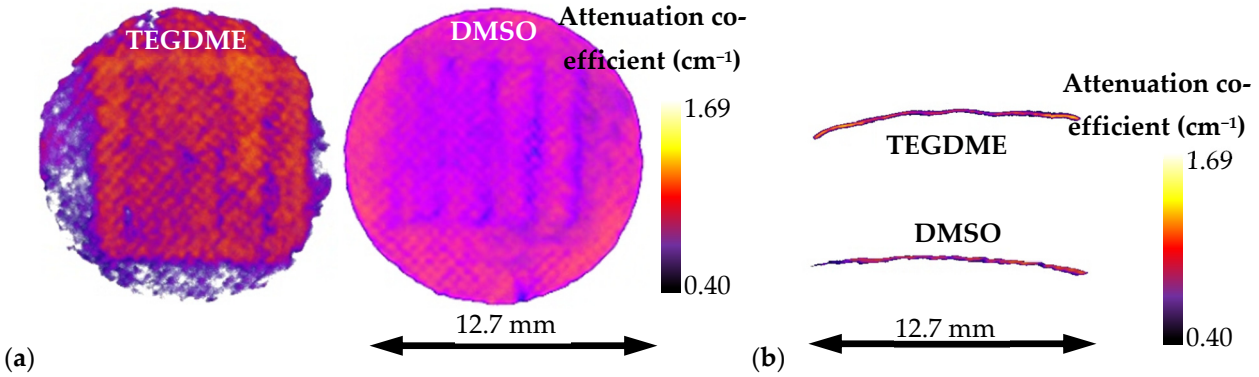


Figure 9. (**a**) Top view of electrodes discharged using TEGDME versus DMSO as the electrolyte at the current density of 0.1 mA/cm^2; (**b**) cross-sectional views along the center of the electrodes.

Additionally, the battery using TEGDME achieved a significantly higher capacity (9.22 mAh/cm^2) compared to the battery using DMSO as the electrolyte (3.65 mAh/cm^2). The neutron imaging data show similar trends, with the average attenuation coefficient of the TEGDME electrode (0.914 cm^{-1}) being higher than those of the DMSO electrode (0.794 cm^{-1}). The attenuation coefficient is determined by scattering and absorption cross-sections of the elements present. Lithium has an exceptionally high neutron attenuation cross-section compared to carbon and oxygen. Therefore, the reconstructed attenuation

coefficient is proportional to the local concentration of Li_2O_2 within the electrode, as described by the Beer–Lambert law:

$$I = I_0 \cdot \exp(-\varepsilon \cdot C \cdot d) \quad (8)$$

where I and I_0 are the transmitted and incident neutron intensities, d is the material thickness, ε is the molar attenuation coefficient, and C is the concentration of Li_2O_2. In addition, the cross-sectional views (Figure 9b) show alternating Li_2O_2 concentrations beneath the channels and ribs. For the TEGDME electrode discharged at 0.1 mA/cm^2, the attenuation coefficient under gas channels is 0.904 cm^{-1}, compared to 0.893 cm^{-1} under ribs. The higher attenuation under the channels indicates a greater concentration of lithium products in those regions. However, the spatial distributions of Li_2O_2 along the thickness direction of the electrodes are not very clear due to the thin electrode thickness and the limited spatial resolution of ~48 μm. For future experiments, using thicker electrodes could better demonstrate the gradients of reaction rates and Li_2O_2 production rates. In future work, we also plan to continue experiments at a neutron facility to achieve a more quantitative analysis of lithium peroxide (Li_2O_2) distribution. Future experiments will use controlled reference samples with precisely controlled amounts of Li_2O_2. These controlled experiments aim to establish a direct correlation between its concentration and the corresponding neutron attenuation coefficient. This calibration will allow us to conduct more qualitative observations and accurately quantify the Li_2O_2 content within our electrochemical samples, providing deeper insights into reaction mechanisms.

At higher current densities (0.25 and 0.5 mA/cm^2), the spatial distributions are not as clear due to a significant capacity reduction with increasing current density. A quantitative analysis of attenuation values generally aligns with the capacity (Li_2O_2 production rates), as shown in the histogram of grayscale values in Figure 10. As shown in the figure, batteries using a DMSO electrolyte achieved capacities of 3.65, 2.76, and 1.68 mAh/cm^2 at current densities of 0.1, 0.25, and 0.5 mA/cm^2, respectively. Correspondingly, the average attenuation coefficients (0.794, 0.653, and 0.560 cm^{-1}) decreased with the decreasing discharge capacity, showing a similar trend.

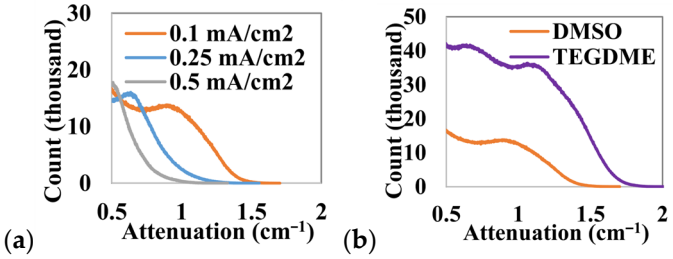


Figure 10. Histogram of attenuation coefficient of (**a**) fully discharged electrodes using DMSO electrolyte at different current densities and (**b**) fully discharged electrodes using DMSO versus TEGDME electrolytes at the discharge current density of 0.1 mA/cm^2.

Comparisons between fully discharged electrodes using the two electrolytes at a discharge current density of 0.1 mA/cm^2 suggest a similar trend. The TEGDME electrode attained a discharge capacity of 9.92 mAh/cm^2, with an average attenuation coefficient of 0.914 (cm^{-1}). In comparison, the DMSO electrode achieved a discharge capacity of 3.65 mAh/cm^2 and an average attenuation coefficient of 0.794 (cm^{-1}). The agreement between the tomography-derived attenuation coefficient and titration measurements confirms that neutron imaging provides not only spatial distribution information but also an accurate bulk quantification of lithium products. This capability of spatially resolved quantification is uniquely enabled by neutron tomography and cannot be achieved through

electrochemical measurements or titration alone. These results suggest that neutron imaging is a powerful tool for battery research, offering quantitative insights into the 3D spatial variations in reaction rates within battery electrodes under different operating conditions. These findings significantly enhance our understanding of electrochemical processes in porous electrodes.

4. Conclusions

This study has experimentally measured and analyzed the dependence of Li-O_2 battery performance and electrochemical reactions on cathode orientation. The cathode orientation with the MPL facing inward, toward the separator, had a higher mass fraction of lithium peroxide, lower discharge and charge capacity, higher activation overpotential, and less stable cycling compared to the MPL facing outward. Additionally, batteries using 1 M LiTFSI/DMSO as the electrolyte show a lower discharge and charge capacity, lower activation overpotential, more stable cycling, and higher effective oxygen diffusivity than 1 M LiTFSI/TEGDME samples. In addition to electrochemical measurements, this study utilized titration methods and unique neutron imaging facilities to quantify the amount of solid product and to analyze its 3D spatial distributions within porous electrodes, respectively. These experiments enhance our understanding of non-uniform electrochemical reactions within electrodes, the effects of different electrolytes, and the impact of various operating conditions.

Author Contributions: H.M.: Data Acquisition, Data Analysis, Writing—Original Draft Preparation; A.S.: Data Acquisition, Data Analysis; Y.N.: Data Acquisition, Data Analysis; Y.Z.: Data Acquisition, Data Analysis, Reviewing, Editing; X.L.: Supervision, Funding Acquisition, Data Acquisition, Data Analysis, Writing—Original Draft Preparation, Reviewing, Editing. All authors have read and agreed to the published version of the manuscript.

Funding: This research was funded by the Advanced Research Projects Agency-Energy (ARPA-E) PROPEL-1K program (Award DE-AR0001884) and the National Science Foundation (Award 1941083 and 2329821).

Data Availability Statement: The original contributions presented in this study are included in the article. Further inquiries can be directed to the corresponding author.

Acknowledgments: The authors acknowledge financial support from Washington University in St. Louis, the Institute of Materials Science and Engineering (IMSE), and Chemical and Environmental Analysis Facility (CEAF) for the use of equipment and staff assistance. X.L. acknowledges Dragonfly for providing the non-commercial license used in this study. A portion of this research used resources at the High Flux Isotope Reactor, a DOE Office of Science User Facility operated by the Oak Ridge National Laboratory. The beam time was allocated to MARS (CG-1D) on proposal number IPTS-35936.1.

Conflicts of Interest: The authors declare no conflicts of interest.

References

1. Kwak, W.-J.; Rosy; Sharon, D.; Xia, C.; Kim, H.; Johnson, L.R.; Bruce, P.G.; Nazar, L.F.; Sun, Y.-K.; Frimer, A.A.; et al. Lithium-Oxygen Batteries and Related Systems: Potential, Status, and Future. *Chem. Rev.* **2020**, *14*, 6626–6683. [CrossRef] [PubMed]
2. Li, X. Li-O_2 flow batteries with high mass loading and energy density. *J. Energy Storage* **2025**, *131*, 117664. [CrossRef]
3. Zubi, G.; Dufo-López, R.; Carvalho, M.; Pasaoglu, G. The lithium-ion battery: State of the art and future perspectives. *Renew. Sustain. Energy Rev.* **2018**, *89*, 292–308. [CrossRef]
4. Njema, G.G.; Ouma, R.B.O.; Kibet, J.K. A Review on the Recent Advances in Battery Development and Energy Storage Technologies. *J. Renew. Energy* **2024**, *2024*, 2329261. [CrossRef]
5. Thackeray, M.M.; Wolverton, C.; Isaacs, E.D. Electrical energy storage for transportation—Approaching the limits of, and going beyond, lithium-ion batteries. *Energy Environ. Sci.* **2012**, *5*, 7854. [CrossRef]

6. Zhang, T.; Sun, H.; Zhang, X.; Wang, X.; Li, J.; Li, Q. Effect of electrolyte level on performance and mass transfer of non-aqueous lithium-oxygen battery. *J. Power Sources* **2024**, *623*, 235425. [CrossRef]
7. Lu, Y.-C.; Gallant, B.M.; Kwabi, D.G.; Harding, J.R.; Mitchell, R.R.; Whittingham, M.S.; Shao-Horn, Y. Lithium-oxygen batteries: Bridging mechanistic understanding and battery performance. *Energy Environ. Sci.* **2013**, *6*, 750–768. [CrossRef]
8. Sarabandi, A.; Adam, A.; Li, X. Influence of Electrolyte Saturation on the Performance of Li–O_2 Batteries. *ACS Appl. Mater. Interfaces* **2024**, *16*, 62902–62913. [CrossRef]
9. Laoire, C.O.; Mukerjee, S.; Abraham, K.M.; Plichta, E.J.; Hendrickson, M.A. Elucidating the Mechanism of Oxygen Reduction for Lithium-Air Battery Applications. *J. Phys. Chem. C* **2009**, *113*, 20127–20134. [CrossRef]
10. Laoire, C.O.; Mukerjee, S.; Abraham, K.M.; Plichta, E.J.; Hendrickson, M.A. Influence of Nonaqueous Solvents on the Electrochemistry of Oxygen in the Rechargeable Lithium−Air Battery. *J. Phys. Chem. C* **2010**, *114*, 9178–9186. [CrossRef]
11. Adams, B.D.; Radtke, C.; Black, R.; Trudeau, M.L.; Zaghib, K.; Nazar, L.F. Current density dependence of peroxide formation in the Li–O2 battery and its effect on charge. *Energy Environ. Sci.* **2013**, *6*, 1772–1778. [CrossRef]
12. Lee, Y.J.; Kwak, W.-J.; Sun, Y.-K.; Lee, Y.J. Clarification of Solvent Effects on Discharge Products in Li–O_2 Batteries through a Titration Method. *ACS Appl. Mater. Interfaces* **2018**, *10*, 526–533. [CrossRef]
13. Sharon, D.; Hirsberg, D.; Salama, M.; Afri, M.; Frimer, A.A.; Noked, M.; Kwak, W.; Sun, Y.-K.; Aurbach, D. Mechanistic Role of Li+ Dissociation Level in Aprotic Li–O_2 Battery. *ACS Appl. Mater. Interfaces* **2016**, *8*, 5300–5307. [CrossRef]
14. Gittleson, F.S.; Jones, R.E.; Ward, D.K.; Foster, M.E. Oxygen solubility and transport in Li–air battery electrolytes: Establishing criteria and strategies for electrolyte design. *Energy Environ. Sci.* **2017**, *10*, 1167–1179. [CrossRef]
15. Li, X.; Huang, J.; Faghri, A. A critical review of macroscopic modeling studies on LiO_2 and Li–air batteries using organic electrolyte: Challenges and opportunities. *J. Power Sources* **2016**, *332*, 420–446. [CrossRef]
16. Zaidi, S.S.H.; Douglas, J.; Li, X. Fluorobenzene-Diluted Localized Highly Concentrated Electrolyte for Enhanced Electrochemical Performance of Li-O_2 Battery. *ACS Appl. Energy Mater.* **2024**, *19*, 8610–8621. [CrossRef]
17. Mohazabrad, F.; Wang, F.; Li, X. Experimental Studies of Salt Concentration in Electrolyte on the Performance of Li-O_2 Batteries at Various Current Densities. *J. Electrochem. Soc.* **2016**, *163*, A2623–A2627. [CrossRef]
18. Santodonato, L.; Bilheux, H.; Bailey, B.; Bilheux, J.; Nguyen, P.; Tremsin, A.; Selby, D.; Walker, L. The CG-1D Neutron Imaging Beamline at the Oak Ridge National Laboratory High Flux Isotope Reactor. *Phys. Procedia* **2015**, *69*, 104–108. [CrossRef]
19. Crow, L.; Robertson, L.; Bilheux, H.; Fleenor, M.; Iverson, E.; Tong, X.; Stoica, D.; Lee, W. The CG1 instrument development test station at the high flux isotope reactor. *Nucl. Instrum. Methods Phys. Res. Sect. Accel. Spectrometers Detect. Assoc. Equip.* **2011**, *634*, S71–S74. [CrossRef]
20. Vo, N.T.; Atwood, R.C.; Drakopoulos, M.; Connolley, T. Data processing methods and data acquisition for samples larger than the field of view in parallel-beam tomography. *Opt. Express* **2021**, *29*, 17849–17874. [CrossRef]
21. Gürsoy, D.; De Carlo, F.; Xiao, X.; Jacobsen, C. TomoPy: A framework for the analysis of synchrotron tomographic data. *J. Synchrotron Radiat.* **2014**, *21*, 1188–1193. [CrossRef]
22. Mäkinen, Y.; Marchesini, S.; Foi, A. Ring artifact reduction via multiscale nonlocal collaborative filtering of spatially correlated noise. *J. Synchrotron Radiat.* **2021**, *28*, 876–888. [CrossRef]
23. Image Processing and Data Analysis Software—Dragonfly. Available online: https://dragonfly.comet.tech/ (accessed on 24 March 2026).
24. Gallant, B.M.; Kwabi, D.G.; Mitchell, R.R.; Zhou, J.; Thompson, C.V.; Shao-Horn, Y. Influence of Li_2O_2 morphology on oxygen reduction and evolution kinetics in Li–O_2 batteries. *Energy Environ. Sci.* **2013**, *6*, 2518–2528. [CrossRef]
25. Mohazabrad, F.; Wang, F.; Li, X. Influence of the Oxygen Electrode Open Ratio and Electrolyte Evaporation on the Performance of Li-O_2 Batteries. *ACS Appl. Mater. Interfaces* **2017**, *9*, 15459–15469. [CrossRef] [PubMed]
26. Li, X.; Faghri, A. Optimization of the Cathode Structure of Lithium-Air Batteries Based on a Two-Dimensional, Transient, Non-Isothermal Model. *J. Electrochem. Soc.* **2012**, *159*, A1747–A1754. [CrossRef]
27. Trahan, M.J.; Mukerjee, S.; Plichta, E.J.; Hendrickson, M.A.; Abraham, K.M. Studies of Li-Air Cells Utilizing Dimethyl Sulfoxide-Based Electrolyte. *J. Electrochem. Soc.* **2012**, *160*, A259. [CrossRef]
28. Rauter, M.T.; Augustin, M.; Spitthoff, L.; Svensson, A.M. Product formation during discharge: A combined modelling and experimental study for Li–O_2 cathodes in LiTFSI/DMSO and LiTFSI/TEGDME electrolytes. *J. Appl. Electrochem.* **2021**, *51*, 1437–1447. [CrossRef]
29. Geaney, H.; O'Dwyer, C. Examining the Role of Electrolyte and Binders in Determining Discharge Product Morphology and Cycling Performance of Carbon Cathodes in Li-O_2 Batteries. *J. Electrochem. Soc.* **2015**, *163*, A43. [CrossRef]

30. Peng, Z.; Freunberger, S.A.; Chen, Y.; Bruce, P.G. A Reversible and Higher-Rate Li-O_2 Battery. *Science* **2012**, *337*, 563–566. [CrossRef]
31. ChemicalBook. Available online: https://www.chemicalbook.com/ (accessed on 24 March 2026).

Disclaimer/Publisher's Note: The statements, opinions and data contained in all publications are solely those of the individual author(s) and contributor(s) and not of MDPI and/or the editor(s). MDPI and/or the editor(s) disclaim responsibility for any injury to people or property resulting from any ideas, methods, instructions or products referred to in the content.